UK Atomic Energy Authority

UKAEA-STEP-CP(23)12

R. T. Osawa, S. L. Newton, D. Moulton, S. S. Henderson, V. Badicel, A. Hudoba

SOLPS-ITER ASSESSMENT OF THE IMPACT OF FUELLING PUFF LOCATIONS ON DIVERTOR IMPURITY RETENTION IN STEP

SOLPS-ITER ASSESSMENT OF THE IMPACT OF FUELLING PUFF LOCATIONS ON DIVERTOR IMPURITY RETENTION IN STEP

R. T. Osawa, S. L. Newton, D. Moulton, S. S. Henderson, V. Badicel, A. Hudoba

This paper has been submitted to
29th IAEA Fusion Energy Conference (FEC 2023), London, 16-21 October 2023

SOLPS-ITER ASSESSMENT OF THE IMPACT OF FUELLING PUFF LOCATIONS ON DIVERTOR IMPURITY RETENTION IN STEP

R.T. OSAWA
UK Atomic Energy Authority
Abingdon, UK
Email: ryoko.osawa@ukaea.uk

S. L. NEWTON, D. MOULTON, S. S. HENDERSON, V. BADICEL, A. HUDOBA
UK Atomic Energy Authority
Abingdon, UK
University of York
York, UK

Abstract

In order to achieve a compatible solution between the divertors and the core, SOLPS-ITER simulations were performed on STEP (Spherical Tokamak for Energy Production) connected double-null geometry to investigate the possibility of using deuterium (D) fuelling puff locations as an actuator for divertor argon (Ar) retention. Significant reduction of upstream Ar density was obtained when D was puffed from outer- and inner-midplanes rather than from private flux regions, which resulted in the orders of magnitude higher Ar compression and enrichment and a factor 4 lower upstream Ar concentration to achieve acceptable target conditions in the investigated parameter range. The key for the significant reduction of upstream Ar density was the induced outflow of middle-charge-state Ar ions such as Ar^{7+}. This outflow was achieved by a combination of D^{+} outflow, high collision frequency, and flipped temperature gradients around the inner midplane. As all of those are effects of the midplane puff, if enough deuterium is puffed from a midplane, one can expect outflow of middle-charge-state Ar ions that increases Ar compression and enrichment by reduction of the upstream Ar density. Further studies should be carried out to investigate if this effect remains desirable despite possible drawbacks such as increased upstream main plasma density.

1. INTRODUCTION

The STEP (Spherical Tokamak for Energy Production) fusion programme [1] aims to produce net energy from a prototype fusion energy plant in the 2040s. One key issue is to achieve a compatible solution between the divertors and the core. One approach to facilitate this is by improving the retention of seeded impurities in the divertor.

The locations of the impurity seeding and the deuterium fuelling are possible actuators for the impurity transport and resulting divertor retention. A study of argon (Ar) seeding location led us to have Ar seeding directly into the scrape-off-layer (SOL) of the inner divertors to increase both the enrichment and compression of Ar on the high-field-side (HFS). As for the deuterium fuelling location, a simulation study on ITER found little impact on divertor conditions in pure hydrogen simulations [2]. However, a more recent study with neon (Ne) seeding showed that Ne retention is improved by main chamber puffing (of both D_2 and Ne) compared to that by private-flux-region (PFR) puffing [3]. Experiments on DIII-D have also demonstrated that deuterium puffing from the SOL improved the impurity retention over divertor puffing [4][5].

To clarify the effect of deuterium fuelling location on Ar retention in a connected-double-null (CDN) geometry, we performed SOLPS-ITER simulations towards optimising the locations in a future STEP design. The locations were set in the PFR, the outer-midplane (OMP), and the inner-midplane (IMP), and four combinations of those were explored. In the following, Sec. 2 describes the modelling setup, Sec. 3 gives overall results, followed by Sec. 4 comparing between specific cases. Section 5 concludes the study with a summary.

2. SOLPS-ITER SETUP AND DEFINITIONS OF COMPRESSION/ENRICHMENT

SOLPS-ITER version 3.0.8 was utilised in this study on the CDN geometry used in [6], with the same plasma species (D and Ar) and simulation settings (e.g. kinetic neutral model, no drifts, constant radial transport coefficients). Most parameters were kept as set in [6], such as the energy flux $P_{\mathrm{in}} = 100\mathrm{MW}$ and the deuterium ion particle flux through the core boundary $\Gamma_{\mathrm{in}} = 3.5 \times 10^{22}\mathrm{s}^{-1}$.

Figure 1 shows the SOLPS-ITER grid and puff/pump locations. Using the 4 locations of D_2 puff in Fig. 1, 4 cases were explored in the study – namely Γ_D^{PFR}, $\Gamma_D^{PFR+OMP}$, $\Gamma_D^{PFR+IMP}$, and $\Gamma_D^{OMP+IMP}$. The fractions of the total D_2 puff injected from each location are shown in Table 1. The rates of D_2 puff and Ar seeding were varied in the ranges $0.6 - 1.6 \times 10^{24} s^{-1}$ and $2.0 - 7.0 \times 10^{21} s^{-1}$, respectively, while the fractions were always kept same.

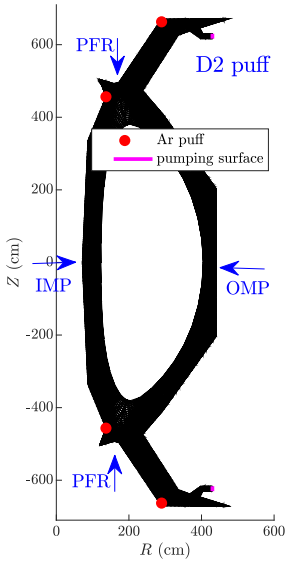

FIG. 1. SOLPS-ITER grid and puff/pump locations.

TABLE 1. EXPLORED CASES

—	Γ_D^{PFR}	$\Gamma_D^{PFR+OMP}$	$\Gamma_D^{PFR+IMP}$	$\Gamma_D^{OMP+IMP}$
PFR	0.5	0.375	0.375	0
PFR	0.5	0.375	0.375	0
OMP	0	0.25	0	0.5
IMP	0	0	0.25	0.5

We define Ar impurity compression C_{Ar} and impurity enrichment E_{Ar} as two measures of the divertor retention, such that

$$C_{Ar} = \frac{n_{Ar,div}}{n_{Ar,up}}, n_{Ar} \equiv n_{Ar0} + \sum_{z=1}^{18} n_{Ar,z+}, \tag{1}$$

$$E_{Ar} = \frac{C_{Ar}}{C_D} = \frac{n_{Ar,div}/n_{D,div}}{n_{Ar,up}/n_{D,up}}, C_D \equiv \frac{n_{D,div}}{n_{D,up}}, n_D \equiv 2n_{D_2} + n_D + n_{D^+}, \tag{2}$$

where $n_{isp,X}$ is the density of species isp in the region X and C_D is the deuterium compression. Divertor SOL region was taken for X=div, while the last-closed-flux-surface (LCFS) was taken for X=up (upstream). To compare the compression and enrichment across the cases that have different puff/seeding rates, the gas puff ratio R was defined as

$$R = \frac{\Gamma_{Ar,puff}}{\Gamma_{Ar,puff} + \Gamma_{D_2,puff} + \Gamma_{D^+,puff}}, \tag{3}$$

where Γ are the particle fluxes from the puffs and through the core boundary.

3. OVERALL RESULT

3.1. Upstream Ar concentration in the operational space/Radiation efficiency

Figure 2 shows direct benefits of $\Gamma_D^{OMP+IMP}$ compared to other cases. Figure 2(a) plots peak target temperature as a function of Ar concentration ($c_{Ar} \equiv n_{Ar}/n_e$) averaged over the last-closed-flux-surface (LCFS), $< c_{Ar,LCFS} >$. The peak target temperature is the maximum temperature of the ions and electrons among all the 4 targets, which was the most critical condition

to obtain an operational space, defined by the peak target temperature < 5 eV and the peak target load ≤ 10 MW/m^2. Comparing $\Gamma_{\rm D}^{\rm OMP+IMP}$ and $\Gamma_{\rm D}^{\rm PFR}$ in the operational space, below the horizontal line, one can see that $\Gamma_{\rm D}^{\rm OMP+IMP}$ achieved the operational space with a factor $\sim$4 lower LCFS Ar concentration than $\Gamma_{\rm D}^{\rm PFR}$. Similarly, as shown in Fig. 2 (b), the same level of total radiation in the SOL is attained with significantly lower LCFS Ar concentration in $\Gamma_{\rm D}^{\rm OMP+IMP}$. As for the intermediate cases, $\Gamma_{\rm D}^{\rm PFR+OMP}$ and $\Gamma_{\rm D}^{\rm PFR+IMP}$, $\Gamma_{\rm D}^{\rm PFR+IMP}$ shows a more significant effect, that is, more reduction of $< c_{\rm Ar,LCFS} >$, than $\Gamma_{\rm D}^{\rm PFR}$.

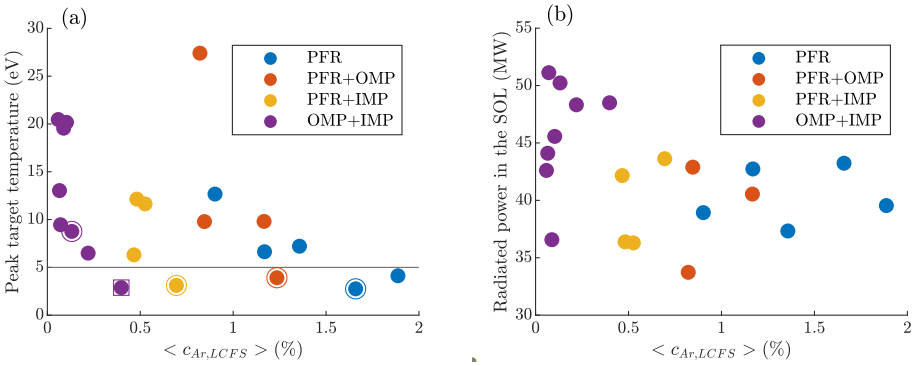

FIG. 2. (a) Peak target temperature v.s. Ar concentration averaged over the last-closed-flux-surface (LCFS), $< c_{\rm Ar,LCFS} >$. (b) Radiated power in the SOL v.s. $< c_{\rm Ar,LCFS} >$.

3.2. Ar compression/enrichment

Figure 3 shows overall results around divertor Ar retention. As shown in Fig. 3(a), $\Gamma_{\rm D}^{\rm OMP+IMP}$ and $\Gamma_{\rm D}^{\rm PFR+IMP}$ have higher Ar compression $C_{\rm Ar}$ than $\Gamma_{\rm D}^{\rm PFR}$ and $\Gamma_{\rm D}^{\rm PFR+OMP}$ on the HFS, which indicates $C_{\rm Ar}$ is enhanced by the presence of the IMP puff, though the enhancement is relatively slight for $\Gamma_{\rm D}^{\rm PFR+IMP}$. As for the low-field-side (LFS), while $\Gamma_{\rm D}^{\rm OMP+IMP}$ again shows higher $C_{\rm Ar}$ than $\Gamma_{\rm D}^{\rm PFR}$ though the effect is smaller than that on the HFS, $\Gamma_{\rm D}^{\rm PFR+OMP}$ shows similar Ar compression to $\Gamma_{\rm D}^{\rm PFR}$ (see Fig. 3(e)). This indicates a weaker enhancement of $C_{\rm Ar}$ is expected from OMP puff compared to IMP puff. Similar trends for $E_{\rm Ar}$ are seen on both sides except that $\Gamma_{\rm D}^{\rm PFR+IMP}$ gives slightly lower values than $\Gamma_{\rm D}^{\rm PFR}$ on the HFS (see Fig. 3(b)). This is due to the higher D compression $C_{\rm D}$ in $\Gamma_{\rm D}^{\rm PFR}$ than in $\Gamma_{\rm D}^{\rm PFR+IMP}$, as shown in Fig. 3 (c). The trend of $C_{\rm Ar}$ ($\equiv n_{\rm Ar,div}/n_{\rm Ar,up}$) comes solely from the upstream Ar density $n_{\rm Ar,up}$ shown in Figs. 3(d) and (h). Although the Ar enrichment on the HFS is more or less affected by D compression, we focus on the Ar compression that shows significant difference between $\Gamma_{\rm D}^{\rm OMP+IMP}$ and the other cases. This leads us to look into the upstream Ar density, which is a starting point of Sec. 4.

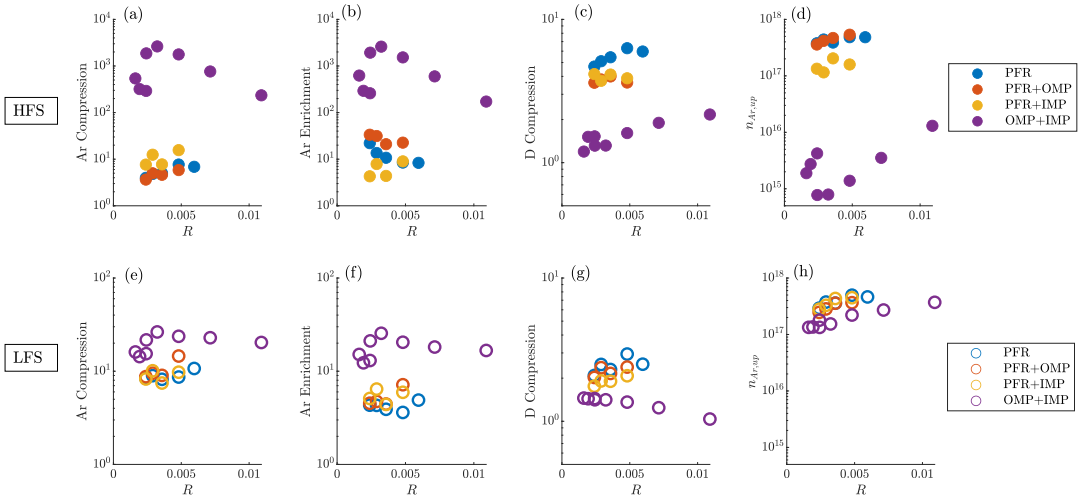

FIG. 3. (a) (e) Ar compression $C_{\rm Ar}$, (b) (f) Ar enrichment $E_{\rm Ar}$, (c) (g) D compression $C_{\rm D}$, (d) (h) upstream Ar density $n_{\rm Ar,up}$ across the cases. The values are averaged over the upper and the lower divertors. (a)-(d): HFS, (e)-(h): LFS.

3.3. Upstream conditions/operational space

For fair comparison, it is preferable to have similar upstream conditions such as the power crossing the separatrix $P_{\rm sep}$ and the midplane separatrix density $n_{\rm e,sep}$. Fig. 4 (a) and (b) show those 2 values for all the cases on the HFS and the LFS, respectively. If we compare the circled markers, the cases with the same D_2 puff and Ar puff rates, $\Gamma_{\rm D}^{\rm OMP+IMP}$ had higher $P_{\rm sep}$ and $n_{\rm e,sep}$ than the other 3 cases on both sides. The high $n_{\rm e,sep}$ is due to the direct ionisation source around the midplane and the high $P_{\rm sep}$ is consistent with the fact that the upstream Ar density is lower for $\Gamma_{\rm D}^{\rm OMP+IMP}$ (see Fig. 2) which leads to lower core Ar radiation. For a fairer comparison, another case with lower D_2 puff and higher Ar puff was obtained to achieve a closer match among the values of $P_{\rm sep}$ and $n_{\rm e,sep}$ – shown by the squared marker. Those 4 cases were selected for further analysis in Sec.4.

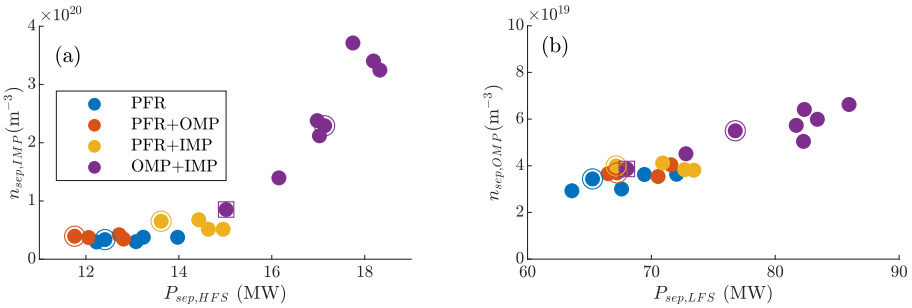

FIG. 4. (a) separatrix electron density at the IMP v.s. power through the HFS separatrix, (b) separatrix electron density at the OMP v.s. power through the LFS separatrix.

It should be noted though that even with the squared-marker case, $n_{\rm e,sep}$ on the HFS is a factor ∼2 higher in $\Gamma_{\rm D}^{\rm OMP+IMP}$ than that in $\Gamma_{\rm D}^{\rm PFR}$. The question is "Is the lower $< c_{\rm Ar,LCFS} >$ (shown in Fig.2(a)) just due to the higher upstream density?". To answer this, we used the control parameter $C = n_{\rm u}\sqrt{c_{\rm Ar}}q_{\parallel \rm u}^{-5/7}$, which determines the level of detachment by the upstream density $n_{\rm u}$, (averaged) Ar concentration $c_{\rm Ar}$, and the upstream parallel energy flux density $q_{\parallel \rm u}$ [7]. Assuming that the detachment level is similar among the 4 selected cases, the Ar concentration should depend on $n_{\rm u}$ and $q_{\parallel \rm u}$ with the relationship $c_{\rm Ar} \propto q_{\parallel \rm u}^{10/7} n_{\rm u}^{-2}$. Figure 5 shows averaged Ar concentration over the LCFS as a function of $P_{\rm sep}^{10/7} n_{\rm sep}^{-2}$ ($P_{\rm sep}$ was used instead of $q_{\parallel \rm u}$ for simplicity as $q_{\parallel \rm u} \propto P_{\rm sep}$) for the HFS (a) and the LFS (b), after being normalised with those values of $\Gamma_{\rm D}^{\rm PFR}$. The markers below the black line mean the Ar concentration is lower than that expected from the changes of the upstream conditions, $n_{\rm sep}$ and $P_{\rm sep}$. Except for $\Gamma_{\rm D}^{\rm PFR+OMP}$ on HFS, one can say that the upstream Ar concentration was reduced from $\Gamma_{\rm D}^{\rm PFR}$ more than expected by the changes of the upstream conditions.

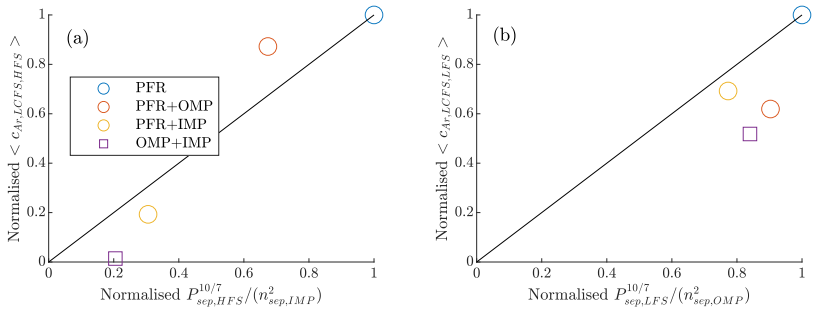

FIG. 5. Ar concentration averaged over the LCFS v.s. $P_{\rm sep}^{10/7} n_{\rm sep}^{-2}$ of the 4 selected cases for (a) HFS and (b) LFS. Both values were normalised to those of $\Gamma_{\rm D}^{\rm PFR}$.

4. ANALYSIS OF AR DENSITY/TRANSPORT IN THE SELECTED CASES

The 4 particular cases, introduced in the previous section and detailed in Table 2, are compared in this section.
Figure 6 shows the density of each charge state of Ar ions averaged over the LCFS on (a) the HFS and (b) the LFS. On the HFS, a pronounced difference starts to appear from Ar^{5+}. In the middle charge states (Ar^{6+} to Ar^{10+}), $\Gamma_{\rm D}^{\rm OMP+IMP}$ has 1-4 orders lower Ar ion density than $\Gamma_{\rm D}^{\rm PFR}$ and $\Gamma_{\rm D}^{\rm PFR+OMP}$. This suggests that the higher compression on the HFS was driven by loss of the middle charge states, which naturally induces the lower Ar density of even higher charge states. On the LFS, a clear difference between the cases is only found in the high charge states, as shown in Fig. 6(b). From Fig. 6, we selected Ar^{7+} to

TABLE 2. SELECTED CASES FOR DETAILED COMPARISON

—	$\Gamma_{\rm D}^{\rm PFR}$	$\Gamma_{\rm D}^{\rm PFR+OMP}$	$\Gamma_{\rm D}^{\rm PFR+IMP}$	$\Gamma_{\rm D}^{\rm OMP+IMP}$
Total D puff ($\times 10^{23}/s$)	10	10	10	6
Total Ar puff ($\times 10^{21}/s$)	5	5	5	7
$n_{\rm sep,OMP}$ ($\times 10^{19}{\rm m}^{-3}$)	3.4	3.7	4.0	3.9
$n_{\rm sep,IMP}$ ($\times 10^{19}{\rm m}^{-3}$)	3.4	4.0	6.5	8.5
$P_{\rm sep}$ (MW)	78	80	81	83

investigate further as it appears to be a key charge state to understand the difference of the upstream Ar density between the cases on the HFS. For clarity, the comparison will focus on $\Gamma_{\rm D}^{\rm PFR}$ and $\Gamma_{\rm D}^{\rm OMP+IMP}$ in the rest of this section.

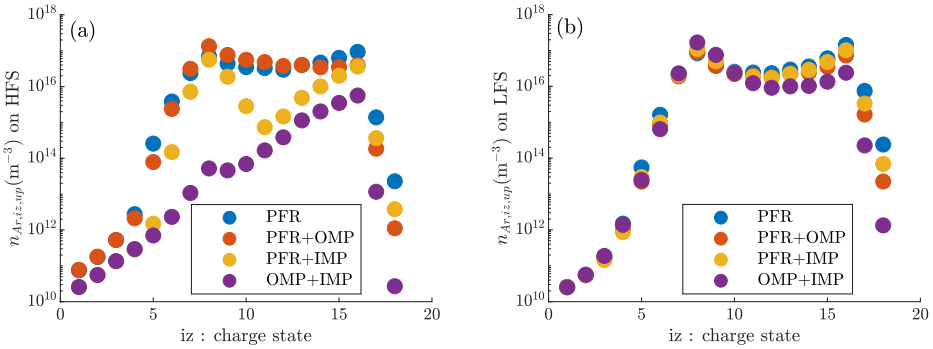

FIG. 6. Density of each charge state of Ar ions averaged in the LCFS on (a) the HFS and (b) the LFS.

To figure out the key factor for the difference of upstream $\rm Ar^{7+}$ density $n_{\rm Ar^{7+},up}$ between $\Gamma_{\rm D}^{\rm PFR}$ and $\Gamma_{\rm D}^{\rm OMP+IMP}$, important terms of the continuity equation of $\rm Ar^{7+}$ are plotted along the second SOL flux tube surrounding the separatrix in Fig. 7 for the HFS (a) and the LFS (b): net particle source (ionisation + recombination) $S_{n_{\rm Ar^{7+}}}$, parallel velocity $V_{\parallel \rm Ar^{7+}}$, parallel particle flux density $n_{\rm Ar^{7+}} V_{\parallel \rm Ar^{7+}}$, and the density $n_{\rm Ar^{7+}}$.

On the HFS, the key factor is $V_{\parallel \rm Ar^{7+}}$. As shown in the top plot of Fig. 7 (a), the net source $S_{n_{\rm Ar^{7+}}}$ is peaking around the divertor entrance for both cases. Then, for the parallel velocity $V_{\parallel \rm Ar^{7+}}$, $\Gamma_{\rm D}^{\rm PFR}$ shows reversed flow (the flow towards IMP) above the divertor entrance whilst it is always directed towards the target in $\Gamma_{\rm D}^{\rm OMP+IMP}$. In $\Gamma_{\rm D}^{\rm PFR}$, the source is mostly transported towards the IMP with the reversed velocity, resulting in relatively high $n_{\rm Ar^{7+},up}$, whilst in $\Gamma_{\rm D}^{\rm OMP+IMP}$, the source is transported towards the target, resulting in low $n_{\rm Ar^{7+},up}$.

Such a difference in $V_{\parallel \rm Ar^{7+}}$ between the two cases is not seen on the LFS. As shown in the second plot of Fig. 7 (b), the magnitude of $V_{\parallel \rm Ar^{7+}}$ is different in the main chamber, yet the flow directions (i.e. locations of the stagnation points) are the same. The smaller magnitude of $V_{\parallel \rm Ar^{7+}}$ in $\Gamma_{\rm D}^{\rm OMP+IMP}$ leads to higher density $n_{\rm Ar^{7+}}$ in the main SOL, but it is compensated by the lower density around the OMP, as shown in the bottom plot of Fig. 7 (b). As a result, there is no significant difference in the integrated density in the main SOL on the LFS.

Given those results, the behaviour of the parallel velocity $V_{\parallel \rm Ar^{7+}}$ – whether it is reversed or not – appears to be the key for having significant reduction of $n_{\rm Ar^{7+},up}$. We investigate $V_{\parallel \rm Ar^{7+}}$ in the next section.

4.1. Analysis of $\rm Ar^{7+}$ velocity

To understand $\rm Ar^{7+}$ velocity behavior, the equation below obtained by assuming $S_{fr,ia} + S_{Therm,ea} + S_{Therm,ia} \sim 0$ in the momentum equation of species a can be used, as was done in [8] (Eq.(25), for SOLPS-4.3):

$$V_{\parallel a} \sim V_{\parallel \rm D^+} + \frac{1}{m_a \nu} \frac{1}{c_{imp}^{(1)}} \left(\frac{c_e^{(2)} c_{\alpha_{ex}}^{(Flim)}}{z_{eff} + \frac{\sqrt{2}}{2}} \frac{\partial T_{\rm e}}{\partial x} + \frac{c_{imp}^{(2)} c_{\alpha_{ab}}^{(Flim)}}{z_{eff_{imp}} + \frac{\sqrt{2}}{2\sqrt{\mu_{aD}/m_D}}} \frac{\partial T_{\rm i}}{\partial x} \right), \quad \nu = \frac{e^4 \ln \Lambda n_D}{6\sqrt{2}\pi^{\frac{3}{2}} \epsilon_0^2 \left(m_a / \sqrt{\mu_{aD}} \right) T_{\rm i}^{\frac{3}{2}}} \quad (4)$$

$S_{{\rm fr},ia}$ is the friction force from the main plasma flow (that by the other Ar ions is neglected here), $S_{{\rm Therm},ea}$ and $S_{{\rm Therm},ia}$ are the thermal force from the electrons and main ions, respectively. Formulae for those forces are nicely summarised in [9][10]. $V_{\parallel a}$ is the parallel velocity of species a, $m_{\rm a}$ is the mass of species a, $\mu_{ab} \equiv m_a m_b/(m_a + m_b)$ is the reduced mass, $T_{\rm e}$ and $T_{\rm i}$ are the electron and ion temperature, $z_{\rm eff} = \sum_{a=0}^{ns-1} z_a^2 n_a / n_e$, $z_{\rm eff,imp} = \sum_{a \in imp} n_a z_a^2 / n_{\rm D^+}$, $c_{imp}^{(1)} =$

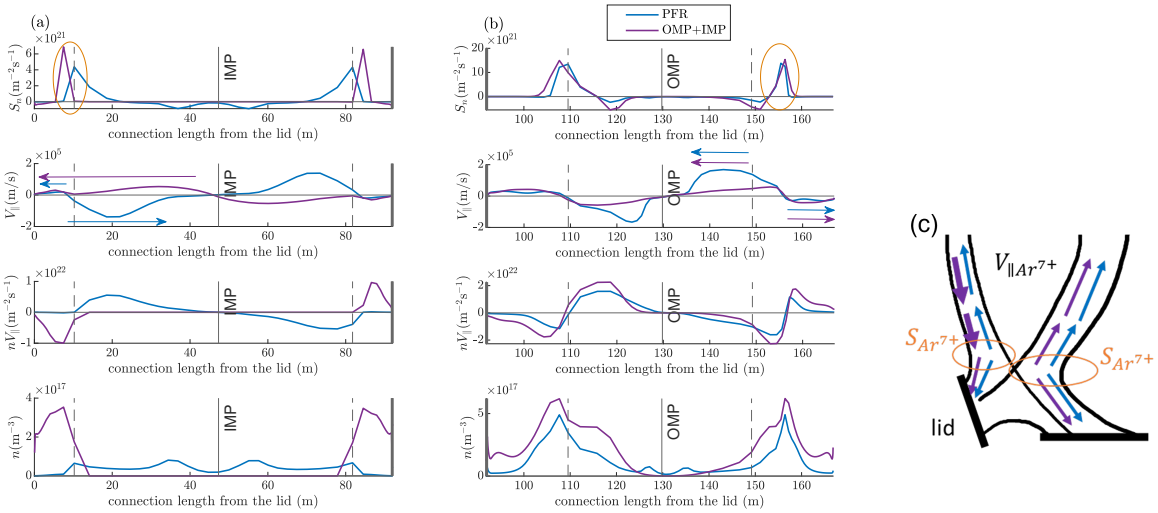

FIG. 7. Profiles of net particle source (ionisation + recombination), parallel velocity, parallel particle flux density, and density of Ar^{7+} along the second flux tube surrounding the separatrix on (a) the HFS and (b) the LFS. The x-axis is the connection length from the lower-inner divertor (lid). (c) Schematic view of the Ar^{7+} parallel velocity from the midplane to the bottom targets. Blue: $\Gamma_{\mathrm{D}}^{\mathrm{PFR}}$, Purple: $\Gamma_{\mathrm{D}}^{\mathrm{OMP+IMP}}$.

$\frac{\left(1+0.24z_{eff_{imp}}\right)\left(1+0.93z_{eff_{imp}}\right)}{\left(1+2.56z_{eff_{imp}}\right)\left(1+0.29z_{eff_{imp}}\right)}$, $c_e^{(2)} = 1.56\frac{(1+1.4z_{\mathrm{eff}})(1+0.52z_{eff})}{(1+2.56z_{\mathrm{eff}})(1+0.29z_{eff})}$, and the flux limiter coefficients $c_{\alpha_{ex}}^{\mathrm{Flim}}$ and $c_{\alpha_{ab}}^{\mathrm{Flim}}$ are assumed to be 1 throughout the analysis in this paper. An important parameter in Eq. (4) is ν, the collision frequency, as it determines how strongly $V_{\|a}$ is impacted by the friction force from the main plasma – with higher ν, it is impacted more by the friction force and less by the thermal force, as confirmed by the fact that $V_{\|a} \sim V_{\|\mathrm{D}^+}$ when $\nu \to \infty$.

Figure 8(a) shows $V_{\|\mathrm{Ar}^{7+}}$ with the black line and $V_{\|\mathrm{D}^+}$ with the orange line for $\Gamma_{\mathrm{D}}^{\mathrm{OMP+IMP}}$ along the second flux tube outside the separatrix. As it was shown in the previous section, the behaviour of $V_{\|\mathrm{Ar}^{7+}}$ is different between the HFS and the LFS, however, that of $V_{\|\mathrm{D}^+}$ is actually similar on both sides. This suggests the difference of the behaviour of $V_{\|\mathrm{Ar}^{7+}}$ between the HFS and the LFS is coming from the second term of Eq. (4)

To separate the effect of ν and the temperature gradients on this second term, the following analysis was conducted on the HFS (see the left plot of Fig. 8(a)). The dashed lines show the right-hand-side (RHS) of Eq. (4) for $\Gamma_{\mathrm{D}}^{\mathrm{OMP+IMP}}$ but replacing the temperature gradients or/and $n_{\mathrm{D}}/T_{\mathrm{i}}^{3/2}$ with those for $\Gamma_{\mathrm{D}}^{\mathrm{PFR}}$. The purple dashed line is the RHS with the temperature gradients replaced. This makes the second term of Eq. (4) negative everywhere as the temperatures monotonically increase from the target to the IMP in $\Gamma_{\mathrm{D}}^{\mathrm{PFR}}$ (see Fig. 8(b)). This leads to reversed flow of $V_{\|\mathrm{Ar}^{7+}}$ near the divertor entrances, but only partially in the main SOL because of the high ν (see Fig. 8(c)). The green dashed line is the RHS with ν replaced instead. Due to the lower ν in $\Gamma_{\mathrm{D}}^{\mathrm{PFR}}$, the magnitude of the second term is large, but there is no flow reversal of $V_{\|\mathrm{Ar}^{7+}}$ as the thermal force around the IMP actually directs to the target. When both the temperature gradients and the collision frequency are replaced with those of $\Gamma_{\mathrm{D}}^{\mathrm{PFR}}$, the estimated $V_{\|\mathrm{Ar}^{7+}}$ in $\Gamma_{\mathrm{D}}^{\mathrm{OMP+IMP}}$, shown with the light-blue dashed line, behaves similar to that for $\Gamma_{\mathrm{D}}^{\mathrm{PFR}}$ – the flow is reversed in the entire main SOL. This analysis confirms that the keys in $\Gamma_{\mathrm{D}}^{\mathrm{OMP+IMP}}$ that changed $V_{\|\mathrm{Ar}^{7+}}$ to that in $\Gamma_{\mathrm{D}}^{\mathrm{PFR}}$ on the HFS are 1) the flipped temperature gradients around the IMP and 2) the higher collision frequency in the main SOL. The factor ~ 100 higher collision frequency $\nu(\propto n_{\mathrm{D}}/T_{\mathrm{i}}^{3/2})$ in $\Gamma_{\mathrm{D}}^{\mathrm{OMP+IMP}}$ than in $\Gamma_{\mathrm{D}}^{\mathrm{PFR}}$ is due to a factor ~ 6 higher n_{D} and a factor ~ 17 higher $T_{\mathrm{i}}^{-3/2}$). Hence, it is fair to say the contribution of the ion temperature is significant to both 1) and 2).

4.2. Impact of the gas puff location on the collision frequency – ion temperature

As discussed in the previous section, the low upstream ion temperature in $\Gamma_{\mathrm{D}}^{\mathrm{OMP+IMP}}$ is an important contributor to the Ar^{7+} upstream density on the HFS. To clarify causes of this, we calculated two estimations of the upstream ion temperature T_{iu}, using the two-point model from an inner divertor target to the IMP. The results are shown in Table 3. The first row shows $T_{\mathrm{iu,tot}}$, integration of the total ion energy flux (conduction and convection) divided by the constant ion parallel heat flux coefficient $\kappa_{\mathrm{i0}\|}^*$ which is assumed to be 50 here. Since the total energy flux is similar between $\Gamma_{\mathrm{D}}^{\mathrm{PFR}}$ and $\Gamma_{\mathrm{D}}^{\mathrm{OMP+IMP}}$, $T_{\mathrm{iu,tot}}$ is similar between the two cases. If we remove the convective ion energy flux from the equation, this gives a clear difference between $\Gamma_{\mathrm{D}}^{\mathrm{PFR}}$ and $\Gamma_{\mathrm{D}}^{\mathrm{OMP+IMP}}$, as shown by $T_{\mathrm{iu,cond}}$ in the second row. In $\Gamma_{\mathrm{D}}^{\mathrm{OMP+IMP}}$, there is a stronger convective flux $q_{\|\mathrm{i,conv}}$ from the IMP to the target than in $\Gamma_{\mathrm{D}}^{\mathrm{PFR}}$, due to the particle flux induced by the ionisation source around the IMP. As

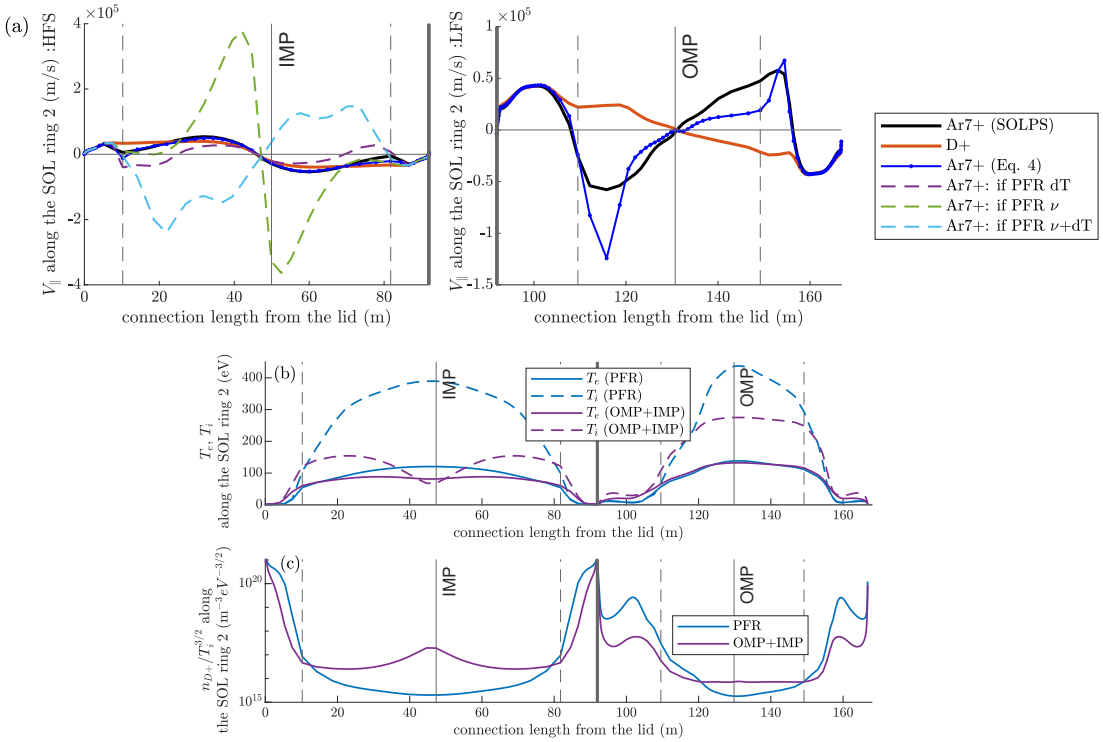

FIG. 8. (a) Analysis of the parallel velocity of Ar^{7+} *along the second flux tube outside the separatrix. (b) Temperature profiles and (c) the variable part of the collision frequency* $n_\mathrm{D}/T_\mathrm{i}^{3/2}$ *of* $\Gamma_\mathrm{D}^\mathrm{PFR}$ *and* $\Gamma_\mathrm{D}^\mathrm{OMP+IMP}$.

the total flux is carried by $q_{\parallel\mathrm{i,conv}}$, $q_{\parallel\mathrm{i,cond}}$ needs to be lower – which reduced $T_\mathrm{iu,cond}$ in $\Gamma_\mathrm{D}^\mathrm{OMP+IMP}$ by a factor ~ 0.5 from $T_\mathrm{iu,tot}$. The third row is the result of the simulations. The deviation of $T_\mathrm{iu,SOLPS}$ from $T_\mathrm{iu,cond}$ should be explained by the fact $q_{\parallel\mathrm{i,cond}} \neq \kappa^*_{\mathrm{i}0\parallel} T_i^{5/2} \frac{\partial T_i}{\partial s}$. The main cause of the inequality is variation of $\kappa_{\mathrm{i}0\parallel}$ - rough estimation gives $\kappa_{i0\parallel} \propto \frac{1}{z_{eff}} \frac{n_D}{n_e}$. Around IMP, $\Gamma_\mathrm{D}^\mathrm{PFR}$ has $z_\mathrm{eff} \sim 7$ and $n_\mathrm{D}/n_\mathrm{e} \sim 0.5$, which gives a factor ~ 10 reduction of $\kappa_{\mathrm{i}0\parallel}$ that estimates a factor ~ 1.9 increase of $T_\mathrm{iu,SOLPS}$ from $T_\mathrm{iu,cond}$. $\Gamma_\mathrm{D}^\mathrm{OMP+IMP}$ does not have such an increase as it has $z_\mathrm{eff} \sim 1$ and $n_\mathrm{D}/n_\mathrm{e} \sim 1$ around IMP. The slightly higher $\kappa_{\mathrm{i}0\parallel}$ than $\kappa^*_{\mathrm{i}0\parallel}$ by a factor 1.5 estimates a factor ~ 0.9 decrease of $T_\mathrm{iu,SOLPS}$ from $T_\mathrm{iu,cond}$. If we compare those factors to the factors given in the third row, however, there is additional reduction of $T_\mathrm{iu,SOLPS}$ from $T_\mathrm{iu,cond}$. This appears to be due to the contribution of anomalous transport which is not negligible in the divertor regions.

To summarise, the lower upstream ion temperature in $\Gamma_\mathrm{D}^\mathrm{OMP+IMP}$ than in $\Gamma_\mathrm{D}^\mathrm{PFR}$ is caused by 1) stronger contribution of the convective energy flux in $\Gamma_\mathrm{D}^\mathrm{OMP+IMP}$ and 2) higher z_eff around IMP in $\Gamma_\mathrm{D}^\mathrm{PFR}$.

TABLE 3. UPSTREAM ION TEMPERATURE ANALYSIS

Equation	T_iu (eV)	
	$\Gamma_\mathrm{D}^\mathrm{PFR}$	$\Gamma_\mathrm{D}^\mathrm{OMP+IMP}$
$T_\mathrm{iu,tot} = \left(\int_t^u \frac{7(q_{\parallel\mathrm{i,cond}}+q_{\parallel\mathrm{i,conv}})}{2\kappa^*_{\mathrm{i}0\parallel}} ds\right)^{2/7}$	280	273
$T_\mathrm{iu,tot} = \left(\int_t^u \frac{7q_{\parallel\mathrm{i,cond}}}{2\kappa^*_{\mathrm{i}0\parallel}} ds\right)^{2/7}$	290 ($\sim 1.04 T_\mathrm{iu,tot}$)	134 ($\sim 0.49 T_\mathrm{iu,tot}$)
$T_\mathrm{iu,SOLPS}$	404 ($\sim 1.39 T_\mathrm{iu,cond}$)	80 ($\sim 0.60 T_\mathrm{iu,cond}$)

5. CONCLUSION

The study showed that deuterium fuelling locations can be an actuator for impurity retention. Among the 4 explored cases under the given parameters in the STEP CDN geometry, namely $\Gamma_\mathrm{D}^\mathrm{PFR}$, $\Gamma_\mathrm{D}^\mathrm{PFR+OMP}$, $\Gamma_\mathrm{D}^\mathrm{PFR+IMP}$, and $\Gamma_\mathrm{D}^\mathrm{OMP+IMP}$, where the superscripts show the locations of the D_2 puff, $\Gamma_\mathrm{D}^\mathrm{OMP+IMP}$ showed significant impact on reducing upstream Ar density on the HFS, which resulted in the orders of magnitude higher Ar compression and enrichment on the HFS compared to $\Gamma_\mathrm{D}^\mathrm{PFR}$. This allowed $\Gamma_\mathrm{D}^\mathrm{OMP+IMP}$ to obtain 1) an operational point and 2) similar total radiation in the SOL with a factor 4 lower upstream

Ar concentration than in $\Gamma_{\mathrm{D}}^{\mathrm{PFR}}$.

The flow velocity of Ar^{7+}, $V_{\|\mathrm{Ar}^{7+}}$, was compared between $\Gamma_{\mathrm{D}}^{\mathrm{OMP+IMP}}$ and $\Gamma_{\mathrm{D}}^{\mathrm{PFR}}$, as Ar^{7+} was a dominant charge state Ar ions that contributed to the reduction of the upstream Ar density in $\Gamma_{\mathrm{D}}^{\mathrm{OMP+IMP}}$. On the HFS, $V_{\|\mathrm{Ar}^{7+}}$ in $\Gamma_{\mathrm{D}}^{\mathrm{OMP+IMP}}$ directed to the targets from the IMP in the entire SOL, while $V_{\|\mathrm{Ar}^{7+}}$ in $\Gamma_{\mathrm{D}}^{\mathrm{PFR}}$ had flow reversal in the main SOL. Hence, the particle source of Ar^{7+} was transported towards targets in $\Gamma_{\mathrm{D}}^{\mathrm{OMP+IMP}}$, resulting in the significantly lower upstream Ar^{7+} density than in $\Gamma_{\mathrm{D}}^{\mathrm{PFR}}$. On the LFS, $V_{\|\mathrm{Ar}^{7+}}$ in the both cases had flow reversal in the main SOL, thus there was no significant difference of the upstream density.

The analysis of $V_{\|\mathrm{Ar}^{7+}}$ showed that 1) higher collision frequency in the main SOL and 2) flipped temperature gradient around the IMP were the keys for $\Gamma_{\mathrm{D}}^{\mathrm{OMP+IMP}}$ to show significant reduction of upstream Ar density compared to $\Gamma_{\mathrm{D}}^{\mathrm{PFR}}$ on the HFS. 1) enhances the friction force from the main plasma whilst 2) changes the direction of the thermal force so it pushes Ar ions towards the targets for $\Gamma_{\mathrm{D}}^{\mathrm{OMP+IMP}}$. The higher collision frequency was due to the higher electron density, originating in the ionisation source from the D_2 puff, and to the lower ion temperature, caused by the convective energy flux enhanced by particle flux from the D_2 puff and the lower z_{eff} due to lower densities of middle/high charge state Ar ions.

We can summarise our findings from this study for future experiments as follows:

- D_2 puff from a midplane can drive the main plasma parallel flow outwards (from the midplane to the divertors), while it tends to be reversed in the main SOL with D_2 puff from PFR – but this not enough for strong impact on Ar distribution.
- The key for strong impact on Ar distribution is the flow of middle charge state Ar ions such as Ar^{7+} - if this is outflow, significant reduction of upstream Ar density can be expected.
- This outflow of Ar^{7+} can be achieved by higher collision frequency which strengthens the friction force from the main plasma flow and/or opposite sign of temperature gradient which flips the thermal force so it pushes Ar ions towards the target. D_2 puff from a midplane can trigger and enhance both effects, thus the strong impact on Ar distribution can be expected to occur when enough D_2 puff is injected from a midplane – IMP puff appears to be more efficient than OMP puff.
- A drawback of a midplane puff can be unavoidable direct effect on the upstream main plasma, such as increasing density and lowering temperature. This might lead to shoulder broadening and resulting higher erosion at the wall, together with enhanced turbulence. If we need to avoid increasing upstream density for such reasons, we could not increase the D_2 puff to enhance divertor neutral pressure. A proposed solution is to carefully balance the negative and positive effects by puffing D_2 from both the PFR and the IMP - the case $\Gamma_{\mathrm{D}}^{\mathrm{PFR+IMP}}$. This setup can potentially reduce the upstream Ar concentration on the HFS, while enhancing divertor neutral pressure without significantly changing the separatrix density.

ACKNOWLEDGEMENTS

This work has been funded by STEP, a UKAEA program to design and build a prototype fusion energy plant and a path to commercial fusion.

REFERENCES

[1] H. Meyer, 29th IAEA Fusion Energy Conference TH-C P/6 2148, London, UK, 16.—21.10.2023.

[2] J-S. Park et al., Nucl. Fusion 61 (2021) 016021.

[3] E. Kaveeva et al., Nuclear Materials and Energy 35, 101424 (2023).

[4] M. R. Wade, et al., J. Nucl. Mater. 266–269 (1999) 44–50.

[5] T. W. Petrie, et al., J. Nucl. Mater. 363–365 (2007) 416–420.

[6] R. T. Osawa, et al., Nucl. Fusion 63 (2023) 076032.

[7] C. Cowley et al., Nucl. Fusion 62 (2022) 086046.

[8] D. Moulton et al., Nucl. Fusion 61 (2021) 046029.

[9] E. Sytova et al., Contrib. Plasma Phys. 58(6–8) (2018) 622–628.

[10] E. Sytova et al., Phys. Plasmas 27 (2020) 082507.